

Probing photonic Bloch wavefunctions with plasmon-coupled leakage radiation

C. J. Regan,^{1,2} O. Thiabgoh,³ L. Grave de Peralta,^{2,3} and A.A. Bernussi^{1,2,*}

¹Department of Electrical and Computer Engineering, Texas Tech University, Lubbock, TX 79409, USA

²Nano Tech Center, Texas Tech University, Lubbock, TX 79409, USA

³Department of Physics, Texas Tech University, Lubbock, TX 79409, USA

*ayrton.bernussi@ttu.edu

Abstract: We demonstrate theoretically and experimentally the direct observation of photonic Bloch wavefunctions in dielectric loaded plasmonic crystals. The ultimate ability to observe the Bloch wavefunctions in the surface emission images depends not on the light diffraction through the holes but on the strength of the in-plane light scattering from the individual lattice features and the presence of the metal layer which allows the light propagating within the crystal to be imaged in the far-field. Experimental results are in excellent agreement with simulated surface emission and back focal plane images of plasmonic crystals.

©2012 Optical Society of America

OCIS codes: (240.6680) Surface plasmons; (160.5293) Photonic bandgap materials; (050.5298) Photonic crystals; (070.7345) Wave propagation.

References and links

1. E. Yablonovitch, "Photonic band-gap structures," *J. Opt. Soc. Am. B* **10**(2), 283–295 (1993).
2. J. D. Joannopoulos, P. R. Villeneuve, and S. Fan, "Photonic crystals: putting a new twist on light," *Nature* **386**(6621), 143–149 (1997).
3. M. Loncar, D. Nedeljkovic, T. P. Pearsall, J. Vuckovic, A. Scherer, S. Kuchinsky, and D. C. Allan, "Experimental and theoretical confirmation of Bloch-mode light propagation in planar photonic crystal waveguides," *Appl. Phys. Lett.* **80**(10), 1689–1691 (2002).
4. N. Le Thomas, R. Houdre, D. M. Beggs, and T. F. Krauss, "Fourier space imaging of light localization at a photonic band-edge located below the light cone," *Phys. Rev. B* **79**(3), 033305 (2009).
5. A. Berrier, M. Swillo, N. Le Thomas, R. Houdre, and S. Anand, "Bloch mode excitation in two-dimensional photonic crystals imaged by Fourier optics," *Phys. Rev. B* **79**(16), 165116 (2009).
6. N. Le Thomas, R. Houdre, M. V. Kotlyar, D. O'Brien, and T. F. Krauss, "Exploring light propagating in photonic crystals with Fourier optics," *J. Opt. Soc. Am. B* **24**(12), 2964–2971 (2007).
7. D. Träger, R. Fischer, D. N. Neshev, A. A. Sukhorukov, C. Denz, W. Królikowski, and Y. S. Kivshar, "Nonlinear Bloch modes in two-dimensional photonic lattices," *Opt. Express* **14**(5), 1913–1923 (2006).
8. S. P. Frisbie, C. Chesnutt, M. E. Holtz, A. Krishnan, L. Grave de Peralta, and A. A. Bernussi, "Image formation in wide-field microscopes based on leakage of surface-coupled fluorescence," *IEEE Photon. J.* **1**(2), 153–162 (2009).
9. D. G. Zhang, X. C. Yuan, and J. Teng, "Surface plasmon-coupled emission on metallic film coated with dye-doped polymer nanogratings," *Appl. Phys. Lett.* **97**(23), 231117 (2010).
10. A. Giannattasio and W. L. Barnes, "Direct observation of surface plasmon-polariton dispersion," *Opt. Express* **13**(2), 428–434 (2005).
11. R. Rodriguez, C. J. Regan, A. Ruiz-Columbié, W. Agutu, A. A. Bernussi, and L. Grave de Peralta, "Study of plasmonic crystals using Fourier-plane images obtained with plasmon tomography far-field superlenses," *J. Appl. Phys.* **110**(8), 083109 (2011).
12. C. J. Regan, A. Krishnan, R. Lopez-Boada, L. Grave de Peralta, and A. A. Bernussi, "Direct observation of photonic Fermi surfaces by plasmon tomography," *Appl. Phys. Lett.* **98**(15), 151113 (2011).
13. A. Krishnan, S. P. Frisbie, L. Grave de Peralta, and A. A. Bernussi, "Plasmon Stimulated Emission in Arrays of Bimetallic Structures Coated with Dye-Doped Dielectric," *Appl. Phys. Lett.* **96**(11), 111104 (2010).
14. S. Randhawa, M. U. González, J. Renger, S. Enoch, and R. Quidant, "Design and properties of dielectric surface plasmon Bragg mirrors," *Opt. Express* **18**(14), 14496–14510 (2010).
15. A. Drezet, A. Hohenau, D. Koller, A. Stepanov, H. Ditlbacher, B. Steinberger, F. R. Aussenegg, A. Leitner, and J. R. Krenn, "Leakage radiation microscopy of surface plasmon polaritons," *Mater. Sci. Engineer. B* **149**(3), 220–229 (2008).
16. I. Gryczynski, J. Malicka, K. Nowaczyk, Z. Gryczynski, and J. Lacowicz, "Effects of sample thickness on the optical properties of surface plasmon-coupled emission," *J. Phys. Chem. B* **108**(32), 12073–12083 (2004).

17. L. Grave de Peralta, R. Lopez-Boada, A. Ruiz-Columbie, S. Park, and A. A. Bernussi, "Some consequences of experiments with a plasmonic quantum eraser for plasmon tomography," *J. Appl. Phys.* **109**(2), 023101 (2011).
 18. A. Houk, R. Lopez-Boada, A. Ruiz-Columbie, S. Park, A. A. Bernussi, and L. Grave de Peralta, "Erratum: "Some consequences of experiments with a plasmonic quantum eraser for plasmon tomography,"" *J. Appl. Phys.* **109**(11), 119901 (2011).
 19. A. N. Grigorenko, A. A. Beloglazov, P. I. Nikitin, C. Kuhne, G. Steiner, and R. Salzer, "Dark-field surface Plasmon resonance microscopy," *Opt. Commun.* **174**(1-4), 151–155 (2000).
 20. G. Stabler, M. G. Somekh, and C. W. See, "High-resolution wide-field surface plasmon microscopy," *J. Microsc.* **214**(3), 328–333 (2004).
 21. C. Kittel, *Introduction to Solid State Physics*, 8th ed. (John Wiley and Sons Inc. 2005).
 22. B. Hecht, H. Bielefeldt, L. Novotny, Y. Inouye, and D. W. Pohl, "Local excitation, scattering, and interference of surface plasmons," *Phys. Rev. Lett.* **77**(9), 1889–1892 (1996).
 23. A. Bouhelier, Th. Huser, H. Tamaru, H. J. Guntherodt, D. W. Pohl, F. Baida, and D. Van Labeke, "Plasmon optics of structured silver films," *Phys. Rev. B* **63**(15), 155404 (2001).
 24. J. D. Joannopoulos, S. G. Johnson, J. N. Winn, and R. D. Meade, *Photonic Crystals: Molding the Flow of Light* (Princeton University Press, 2008).
 25. RSoft Corporation, <http://www.rsoftdesign.com>.
-

1. Introduction

Light propagation in periodic artificial structures such as photonic crystals has been the subject of great interest from both the fundamental and the applied standpoints. The ability to generate, guide, confine and detect light in the nanoscale with photonic periodic structures lead to the realization of a new generation of compact optical and optoelectronic devices with unprecedented functionalities [1, 2]. The interaction of electromagnetic waves with photonic periodic structures is described by the well-known Bloch wavefunctions. Experimental determination of Bloch wavefunctions is an invaluable diagnostic tool to obtain detailed information about the periodic structure including dispersion relation and image formation. Indirect and direct experimental verification of Bloch wavefunction dispersion in photonic crystal slab waveguides were demonstrated experimentally by out-of-plane leakage of light and by near-field optical microscopy, respectively [3–6]. More recently the non-linear dispersion of Bloch wavefunctions was theoretically and experimentally investigated by selective excitation of the Bloch waves in photonic crystals at the high-symmetry points [7]. Although those studies provide fundamental information about the Bloch wavefunction propagation in photonic crystals, their realization requires special sample fabrication, dedicated technique, or special excitation conditions which limit the range of the available Bloch modes that are excited within the sample. In addition, to the best of our knowledge, no investigation on the influence of Bloch wavefunction dispersion on the image formation of photonic or plasmonic periodic structures has been reported thus far.

Experimental [8–14] and theoretical [12, 14] studies of back focal plane (BFP) images of plasmonic crystals using plasmon coupled leakage radiation (PCLR) [8, 15–18] have been reported by several groups. Several studies involving real plane images of plasmonic crystals using plasmon-related imaging techniques have also been discussed [8, 19, 20]. More recently it has been reported the observation of periodic nanosize features in the surface emission (SE) images of plasmonic crystals obtained by the PCLR technique [11]. However, no detailed analysis or explanation of the subwavelength capabilities of this imaging technique has been reported.

In this paper we present a detailed investigation on the mechanisms involved in imaging a plasmonic crystal's Bloch wavefunctions using the PCLR technique. We demonstrate for the first time that the SE image of dye-doped dielectric-loaded plasmonic crystals can be described by an incoherent superposition of photonic Bloch wavefunctions involving all possible grating vectors of the crystal reciprocal lattice. We verified that the strength of the in-plane scattering of light at the holes within the plasmonic crystals determines the SE image contrast of plasmonic crystals. Our simulations are supported by experiments based on SE and BFP images of dye-doped dielectric-loaded plasmonic crystals. Compared to previous studies, our method allows for unparalleled clarity of imaging of all allowed propagating modes, through the high-efficiency out-coupling of the light as well as the isotropic mode excitation

method using fluorescent dyes, which cannot be directly applied to conventional photonic crystals.

2. Theory

A Bloch electromagnetic wavefunction is a spatially periodic function which is a monochromatic and amplitude-modulated plane wave, and has the property of being transmitted through a medium of periodic dielectric constant as a result of constructive interference of scattered wave-fronts. The phasor form of a Bloch wavefunction ($\psi_{\vec{k}}(\vec{r})$) can be defined at a single wavevector \vec{k} as [21]:

$$\psi_{\vec{k}}(\vec{r}) = u_{\vec{k}}(\vec{r}) \cdot e^{j\vec{k} \cdot \vec{r}} \quad (1)$$

where $u_{\vec{k}}(\vec{r})$ is a function of the position vector \vec{r} with periodicity equal to the periodicity of the lattice which can be represented by a Fourier series in the form [21]:

$$u_{\vec{k}}(\vec{r}) = \sum_{\vec{G}} c_{\vec{k},\vec{G}} \cdot e^{j\vec{G} \cdot \vec{r}} \quad (2)$$

where \vec{G} represents all the possible grating vectors of the crystal reciprocal lattice and $c_{\vec{k},\vec{G}}$ are the Fourier coefficients. Substituting Eq. (2) into Eq. (1) yields the form for the Bloch function at a specific value of \vec{k} :

$$\psi_{\vec{k}}(\vec{r}) = \sum_{\vec{G}} c_{\vec{k},\vec{G}} \cdot e^{j(\vec{G}+\vec{k}) \cdot \vec{r}} \quad (3)$$

If we assume transverse-electric (TE) polarized plane waves in the x - z plane of the form Eq. (3) then the electric field component in the y -direction (E_y) can be expressed as:

$$E_{y_{\vec{k}}}(\vec{r}) = \text{Re} \left[\psi_{\vec{k}}(\vec{r}) \right] \quad (4)$$

The corresponding intensity ($I_{\vec{k}}$) of a photonic Bloch wavefunction $\psi_{\vec{k}}(\vec{r})$ can be calculated as

$$I_{\vec{k}} = |\psi_{\vec{k}}(\vec{r})|^2 = u_{\vec{k}}^2(\vec{r}) \quad (5)$$

The total intensity I corresponding to the incoherent superposition of several photonic Bloch wavefunctions is equal to the sum of the intensities $I_{\vec{k}}$ over all possible \vec{k} -values. From Eq. (5) we conclude that the intensity of a photonic Bloch wavefunction will always have a periodicity equal to that of the lattice. However, it should be pointed out here that depending on the values of \vec{k} , E_y may or may not have the same periodicity as that of the crystal lattice.

Photonic Bloch wavefunctions are of particular interest because they carry information about the lattice (and defects), and they are dependent exclusively on the in-plane scattering to carry that information. However, most photonic Bloch modes are completely vertically confined and cannot be imaged without the use of near-field scanning techniques or other complex out-coupling and imaging methods [3–7]. PCLR [8, 9, 15, 22, 23], on the contrary, is ideal for investigating photonic Bloch modes in the far-field. The leaked light provides back focal plane (BFP) images corresponding to the momentum map of the photons traveling in the surface of the plasmonic crystal [10]. The metal layer used in the realization of plasmonic crystals, specifically, causes the mode to have a term of propagation perpendicular to the guiding layer. This can be used to transform a strictly near-field phenomenon into a far-field one.

Typical BFP images of plasmonic crystals consist of several sets of rings, where the radius is proportional to the value of \vec{k} at that point [10]. Each circle is displaced from the others by the reciprocal crystal lattice vectors \vec{G} . This implies that each bright intensity point in the BFP image represents one value of the vector $(\vec{k} + \vec{G})$ in the summation in Eq. (3). In the SE image obtained from the Fourier transform of the BFP, Eq. (5) applies: as the light leaks to the substrate from every point of the metal-glass interface, the intensity distribution observed in the SE image is proportional to the total intensity (sum of $I_{\vec{k}}$). This implies that in order to image the Bloch function, all that is needed is the extra rings in the BFP. This information is only dependent on the in-plane scattering adding momentum \vec{G} to individual photons that propagate at the interface, and will be contained in the leaked light via its angle of leakage. Therefore, imaging of the Bloch wavefunction will be independent of the diffraction through the holes within the crystal. In fact, imaging of the Bloch wavefunction can be also obtained for nanosize holes [11]. It is important to note here that while the surface features may be extremely small, the SE image will correspond to the Bloch wavefunction and not to the surface itself. Although the details of individual features with very small sizes within the crystal may not be clearly distinguishable, the crystal periodicity signature in the SE images can be verified even for feature sizes far smaller than that expected from the diffraction limit of the light [11]. There are, of course, limitations to this technique. For example, the holes must be of sufficient size so that there is non-negligible in-plane scattering. Specifically this implies that the value $c_{\vec{k},\vec{G}}$ in (2), for $\vec{G} \neq 0$, is a significant fraction of the total sum. Smaller holes will result in reduced image contrast. The scattering features must also be arranged periodically, with a period within the limit $p > \lambda_{\text{SPP}}/2$ [24]. Finally, a metal sheet must be included so that the excited photonic Bloch modes can leak to the substrate and then be imaged in the far-field.

In order to provide supporting evidence that the SE images of plasmonic crystals actually correspond to the total intensity associated with an incoherent superposition of photonic Bloch modes rather than the surface itself, we measured the SE images of dye-doped dielectric-loaded plasmonic crystals using the PCLR technique and then compare the obtained results with the simulated intensity of the photonic Bloch wavefunctions of the same plasmonic crystals for several values of \vec{k} for all possible \vec{G} values.

3. Sample fabrication

The samples used in this work consisted of ~110 nm thick Rhodamine-6G (R6G) doped PolyMethylMethAcrylate (PMMA) spun on top of a 50 nm thick gold film which was deposited on a glass substrate. The PMMA was patterned into a square symmetry crystal lattice with 200 nm hole diameter (d) and 350 nm period (p). Figure 1 shows a schematic (a) and Scanning Electron Microscope (SEM) top view image (b) of the fabricated crystal. The dye molecules were excited using a 532 nm wavelength laser source focused on the top of the sample by a 40 × microscope objective lens to the approximate size of the patterned plasmonic crystal. The emitted fluorescence from the dye molecules occurs in all directions and has peak intensity centered at ~568 nm wavelength. Part of the emitted light couples to surface plasmon photonic Bloch modes at the gold-PMMA interface. Details of the PCLR technique used can be found in [8]. The plasmon coupled light leaks to the glass substrate and then is collected by a 100 × microscope objective lens, bandpass filtered at 568 nm wavelength, and imaged in the

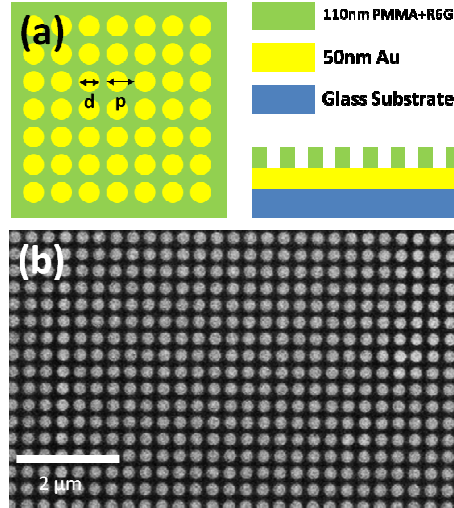


Fig. 1. Schematic (a) and SEM top view (b) of the fabricated dye-doped dielectric-loaded plasmonic crystal.

real plane. The microscope objective lens produces the BFP, where we can then obtain the corresponding momentum map of the photons propagating in the surface of the crystal.

4. Results and discussion

We simulated the SE images of plasmonic crystals by evaluating $u_{\vec{k}}^2(\vec{r})$, as described in Eq. (5). A summation is performed over all possible \vec{G} values where each $u_{\vec{k}}(\vec{r})$ has a different value for every allowed \vec{k} . The function $u_{\vec{k}}^2(\vec{r})$ will have a periodicity equal to that of the lattice for each \vec{k} , since its periodicity is only dependent on \vec{G} . However, the total intensity of $I_{\vec{k}}$ may differ for different directions of \vec{k} , and may not be the same in the x - and z -directions for a given \vec{k} -value. This is because the Fourier coefficients $c_{\vec{k},\vec{G}}$ have some dependence on both k_x and k_z . Since $c_{\vec{k},\vec{G}}$ is complex valued it can also introduce a phase shift.

Due to the finite numerical aperture of the microscope objective collecting lens (NA = 1.49) used in our experiments, the grating vectors \vec{G} in the x - and z -directions in the BFP images of the plasmonic crystals investigated here are restricted to $-1 \leq G_x \leq 1$ and $-1 \leq G_z \leq 1$. This corresponds to a total of nine rings in the BFP images of square lattice plasmonic crystals (see discussion below). From Eq. (3) and Eq. (5) and the possible \vec{G} -values we can then determine the corresponding intensity of the experimental SE images as:

$$I = \sum_{\vec{k}} I_{\vec{k}} = \sum_{\vec{k}} \left| \sum_{G_x=-1}^1 \sum_{G_z=-1}^1 c_{\vec{k},\vec{G}} \cdot e^{j(G_x x + G_z z)} \right|^2 \quad (6)$$

Figure 2(a) shows the simulated BFP image, or equifrequency plot, of a square lattice plasmonic crystal with hole diameter 200 nm and periodicity 350 nm. The simulations were performed using the commercial software package BandSolveTM from RSoft [25]. The high-symmetry points in the crystal reciprocal momentum space are also indicated in Fig. 2(a). The simulated BFP image consists of a central ring and eight shifted rings corresponding to, respectively, the guided wave plasmon-coupled propagation mode and to direct images of the photonic Fermi surfaces centered at each reciprocal lattice point, with center-to-center separation determined by the crystal lattice vectors [12]. The First Brillouin Zone (FBZ) is

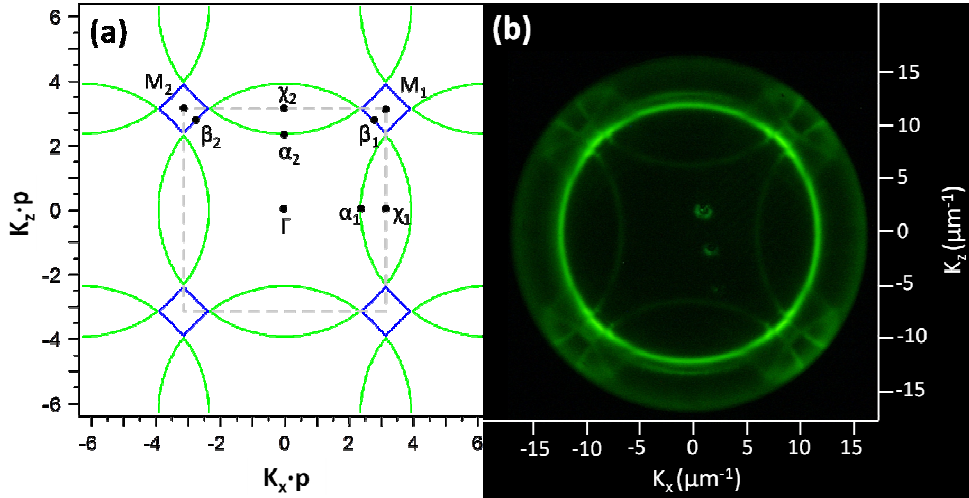


Fig. 2. Simulated (a) and experimental (b) BFP images of a square lattice with hole diameter $d = 200$ nm and period $p = 350$ nm. In (a) we indicate the most relevant points in the reciprocal space.

also indicated in Fig. 2(a) by a dashed line. The experimental BFP image of a plasmonic crystal with identical dimensions as that used in the simulation (Fig. 2(a)) is shown in Fig. 2(b). The close agreement between simulated and experiment is evident from the BFP images shown in Fig. 2. The high-symmetry points Γ , χ , and M of the crystal reciprocal momentum space in Fig. 2(a) are defined similarly to those used in the study of solid state and purely dielectric photonic crystals. Then we denote α and β as the points along the irreducible FBZ edge which intersect the mode of interest in the $\Gamma - \chi$ and $\Gamma - M$ directions, respectively. In our analysis we specifically evaluated $I_{\vec{k}}$ at multiple α and β points with different k_x and k_z values so that any effect of the $c_{\vec{k}, \vec{G}}$ Fourier coefficients on the SE image formation are taken into account.

Figures 3(a)-3(c) show the corresponding simulated photonic Bloch surface mode intensities given by Eq. (6), for $\vec{k} = \alpha_1, \beta_1$, and for the summation approximation of the total intensity $I_{\alpha_1} + I_{\beta_1} + I_{\alpha_2} + I_{\beta_2}$, respectively, for a plasmonic crystal with the same dimensions used to obtain Fig. 2(a). The period is normalized to one so that the lattice points exist at every integer value. We also show in Fig. 3(d) the experimental SE image of a fabricated plasmonic crystal which corresponds to the simulated total intensity image shown in Fig. 3(c). Figure 3(a) clearly shows that at α_1 point there exist differences in the amplitude of $I_{\vec{k}}$ in the z - and x -directions, while the periodicity is the same in both the z - and x -directions. This is expected from Eq. (6), since the periodicity is dependent only on \vec{G} , while the intensity depends on both \vec{G} and \vec{k} . In Eq. (6) at α_1 , \vec{G} includes both G_x and G_z , while \vec{k} includes only k_x . This specifically justifies why it is necessary to evaluate $I_{\vec{k}}$ for both α_1 and α_2 , where each point will be rotated by 90 degrees with respect to each other. In Fig. 3(c) we simulate the sum of the intensities at points $\alpha_1, \alpha_2, \beta_1$, and β_2 . This summation approximates Eq. (6) by including all allowed \vec{G} vectors and includes the most important \vec{k} vectors: those found on the high symmetry lines (see Fig. 2(a)). This is only an approximation of the experimental data shown in Fig. 3(d) since it does not include all \vec{k} values, rather only at α and β , and also includes more \vec{G} values than those accounted for in Eq. (6).

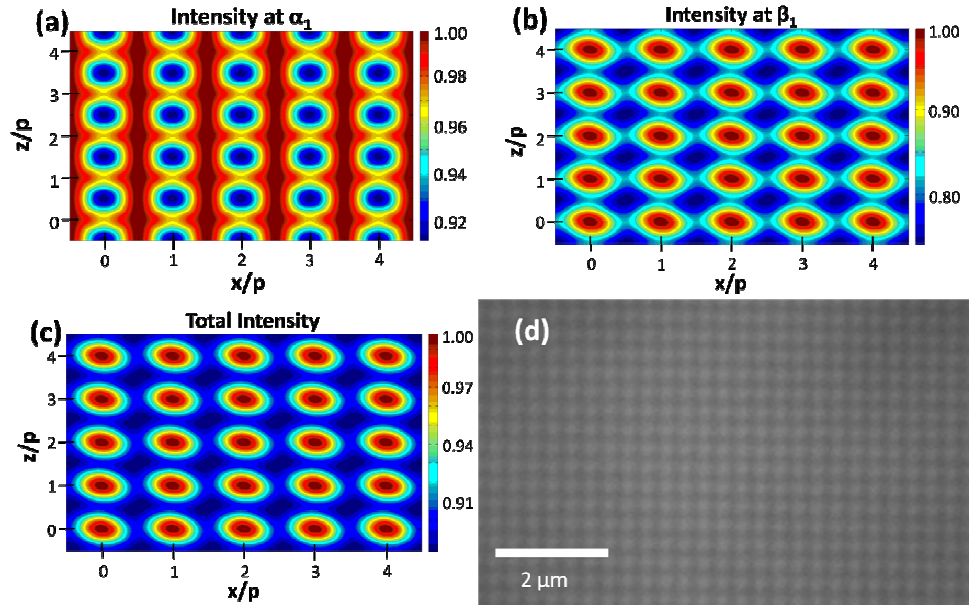


Fig. 3. Simulated photonic Bloch function images, using Eq. (5), evaluated at (a) α_1 , (b) β_1 , and (c) at the summation of α_1 , β_1 , α_2 , and β_2 . Simulated images are normalized to the period. (d) Experimental SE image of a square lattice plasmonic crystal with the same symmetry and dimensions used in the simulations (a)-(c).

However, it is evident from Figs. 3(c) and 3(d) that a good agreement exists between simulations and experiment. Furthermore, a comparison between Figs. 3(d) and 1(b) demonstrates that the SE image obtained by PCLR technique permits observation of the subwavelength periodic features of the fabricated sample well. In order to further support this claim we show in Fig. 4 an intensity line profile along the x -direction over several crystal periods for the SE image shown in Fig. 3(d). The small periodic variation observed in Fig. 4 may be attributed to fluctuations in the periodicity of the fabricated plasmonic crystal while the larger intensity variations are attributed to non-uniform excitation of the fluorescent dye.

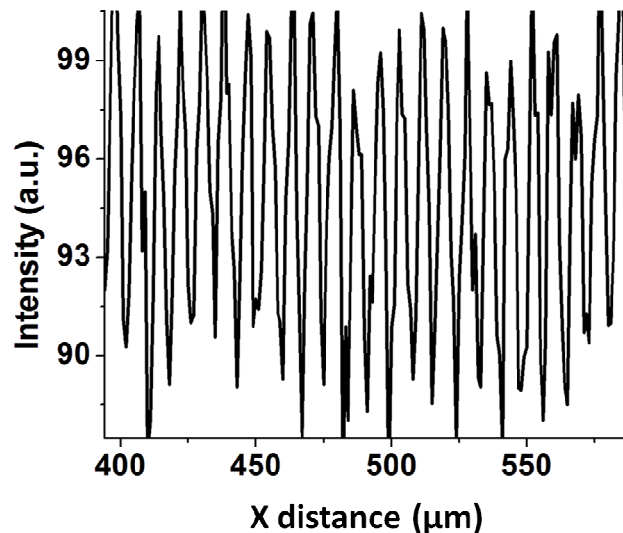


Fig. 4. Intensity line profile plot of the SE image shown in Fig. 3(d).

We determined from Fig. 4 that I_k varies from 88% to 100%, which almost exactly matches the simulated intensity variation shown in Fig. 3(c), suggesting that the summation at

the points α_1 , α_2 , β_1 , and β_2 is a good approximation for Eq. (6). While we have shown imaging capabilities down to nanoscale holes [11], here we choose to use larger holes to unambiguously demonstrate that photonic Bloch wavefunctions can be imaged in dye-doped plasmonic crystals with plasmon-coupled leakage radiation.

In order to provide additional supporting evidence that the SE images of plasmonic crystals are directly related to the photonic Bloch functions described here, we can isolate the components of \vec{G} in the BFP, specifically allowing only one value of the grating vector in (6). In this case the intensity now takes the form:

$$I = \sum_{\vec{k}} I_{\vec{k}} = \sum_{\vec{k}} \left| \sum_{G_x=-1}^1 c_{\vec{k}, \vec{G}} \cdot e^{j(G_x x + G_z z)} \right|_{G_z=0}^2 \quad (7)$$

We can visualize Eq. (7) as taking Eq. (6) and only including values of \vec{G} in the x -direction. Experimentally, we can achieve this effect by placing a spatial filter with a narrow transmission slit in the x -direction in the BFP of the collecting microscope objective lens. We can also introduce the slit in the reciprocal lattice diagonal so that Eq. (6) becomes:

$$I = \sum_{\vec{k}} I_{\vec{k}} = \sum_{\vec{k}} \left| \sum_{G_x=-1}^1 \sum_{G_z=-1}^1 c_{\vec{k}, \vec{G}} \cdot e^{j(G_x x + G_z z)} \right|_{G_x=G_z}^2 \quad (8)$$

following the constraint $G_x = G_z$. In these cases we now expect the periodicity of the SE images to become one-dimensional in the x -direction and in the diagonal direction $(x+z)/\sqrt{2}$, respectively.

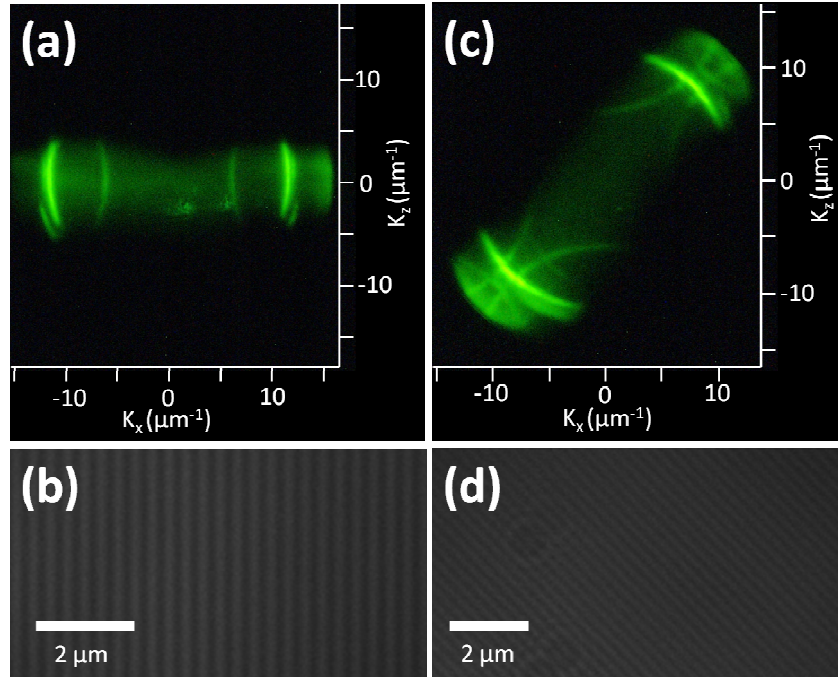


Fig. 5. BFP ((a) and (c)) and SE ((b) and (d)) images obtained using a spatial slit filter placed in the BFP of the collecting microscope objective lens. This filter restricts which components of the vector \vec{G} will be imaged at the surface.

Figure 5 shows the results of these experiments: when the slit is placed parallel to the x -direction in the BFP image (Fig. 5(a)) the SE image (Fig. 5(b)) consists of vertical parallel lines with period equal to that of the crystal lattice. Similar results (not shown) were obtained when the filter slit is placed in the z -direction, but in this case horizontal parallel lines were observed. When the slit is placed at a 45° degree angle in the BFP (Fig. 5(c)) the SE image (Fig. 5(d)) consists of tilted (45° degrees) parallel lines. It is important to note here that for these cases the holes' signature in the SE images disappears and parallel lines are observed instead. We determined from Figs. 5(b) and 5(d) line periods (p) of $p = 354 \pm 4$ nm and $p = 250 \pm 4$ nm, which are in excellent agreement with the designed lattice periodicity (350 nm) and the expected period along the diagonal (254 nm) which is defined as $p / \sqrt{2}$, respectively. The results shown in Fig. 5 further confirm that the SE images of dye-doped dielectric-loaded plasmonic crystals results from the incoherent superposition of photonic Bloch wavefunctions propagating at different crystal reciprocal lattice vectors rather than the surface itself.

5. Conclusions

We have investigated analytically, numerically, and experimentally photonic Bloch functions in dye-doped dielectric-loaded plasmonic crystals using surface plasmon-coupled leakage radiation technique. Our results indicate that the images observed in the plasmonic crystals are due to a combination of incoherent superposition of photonic Bloch wavefunctions as a result of the crystal periodicity, in-plane light scattering at the lattice patterned holes, and due to the presence of the thin metal layer which enables the propagating light within the crystal to leak into the substrates and then be imaged in the far-field. Excellent agreement between simulated and measured SE and BFP images of plasmonic crystals were obtained. Compared to previous studies, our approach enables well-defined SE and BFP images and allows light coupling to all available Bloch modes within the crystal. Furthermore, we provide a theoretical explanation for previously observed PCLR-SE images of plasmonic crystals with feature sizes well below the diffraction limit of the light.

Acknowledgments

This work was partially supported by the NSF CAREER Award (ECCS-0954490).